ANTIOXIDANTS & REDOX SIGNALING
Volume 9, Number 8, 2007

DOI: 10.1089/ars.2007.1638

Forum Review

Spatially Resolved Biologic Information from *In Vivo* EPRI, OMRI, and MRI

KEN-ICHIRO MATSUMOTO,[1,2] SANKARAN SUBRAMANIAN,[1]
RAMACHANDRAN MURUGESAN,[1] JAMES B. MITCHELL,[1] and MURALI C. KRISHNA[1]

ABSTRACT

EPR spectroscopy can give biologically important information, such as tissue redox status, pO_2, pH, and microviscosity, based on variation of EPR spectral characteristics (*i.e.*, intensity, linewidth, hyperfine splitting, and spectral shape of free radical probes. EPR imaging (EPRI) can obtain 1D–3D spatial distribution of such spectral components using several combinations of magnetic field gradients. Overhauser enhanced MRI (OMRI) is a double-resonance technique of electron and nuclear spins. Because the Overhauser enhancement depends on transverse relaxation rate of the electron spin, OMRI can provide pO_2 information indirectly, along with a high-resolution MR image. MRI can also indirectly detect paramagnetic behaviors of free radical contrast agents. Imaging techniques and applications relating to paramagnetic species (*i.e.*, EPRI, OMRI, and MRI) have the potential to obtain maximally 5D information (*i.e.*, 3D spatial + 1D spectral + 1D temporal dimensions, theoretically). To obtain suitable dimensionality, several factors, such as the EPR spectral information, spatial resolution, temporal resolution, will have to be taken into account. For this review, the EPRI, OMRI, and MRI applications for the study biological systems were evaluated for researchers to apply the method of choice and the mode of measurements to specific experimental systems. *Antioxid. Redox Signal.* 9, 1125–1141.

INTRODUCTION

SEVERAL IMAGING TECHNIQUES have been used clinically to visualize the anatomy of human patients or experimental animals or both noninvasively. Anatomic imaging techniques, such as x-ray computed tomography (CT) and magnetic resonance imaging (MRI) can provide anatomic information.

MRI can show not only anatomic information but also the effects of proton relaxation time as contrast. Several pulse sequences have been developed to examine the effects of T_1, T_2, T_2^*, or M_0. The difference of the MR image contrast obtained before and after a cognitive task can impart biologic functional information to the MR image, which is called functional MRI (*f*MRI) or blood oxygen level–dependent MRI (BOLD-MRI) (84). More recently, we have reported tissue oxygen level–dependent MRI (TOLD-MRI) (76). This method detects enhancement of T_1-weighted contrast in the tissue, which is due to direct T_1-shortening by the paramagnetic molecular oxygen. A combination of a paramagnetic contrast agent and a time sequence of T_1-weighted MRI scan can show the pharmacokinetics of the paramagnetic contrast agent. With a redox-sensitive contrast agent, such as nitroxyl radicals, the redox status in tissue can be estimated (75).

Electron paramagnetic resonance imaging (EPRI) requires relatively stable free radicals, such as nitroxyl radicals, triarylmethyl (TAM) radicals, or paramagnetic particles as spin probes. In the continuous-wave (CW) modality, information of spatial distributions of the spin probes is encoded in the EPR

[1]Radiation Biology Branch, Center for Cancer Research, National Cancer Institute, National Institutes of Health, Bethesda, Maryland.
[2]Heavy-Ion Radiobiology Research Group, Research Center for Charged Particle Therapy, National Institute of Radiological Science, Chiba 263-8555, Japan.

spectrum using a static field gradient (1D spatial information). However, EPR spectral information, such as linewidth and hyperfine splitting, are still retained in the EPR spectrum under the gradient. Therefore, the EPR spectral information has to be deconvolved from the projection data to reconstruct a pure spatial image of the spin probe. Rotation of the field gradient can give a projection data set to obtain 2D or 3D EPR image.

A systematic variation of field-gradient amplitudes on the each direction of the gradient provides an additional spectral dimension to reconstruct the pseudo spectral–spatial image matrix. CW EPR spectral–spatial image-reconstruction technique can give local spectral information as a reconstructed 2D, 3D, or 4D spectral–spatial image matrix. Therefore, local environments encountered by the spin probe can be obtained from EPR spectra, enabling molecular functional mapping capability. Although data acquisition by time-domain EPRI is similar to MRI, the data obtained by the time-domain EPR are basically same as CW EPR, except that the data is Fourier transformed (70, 102). The data obtained by time-domain EPR is manipulated in k-space to obtain 2D, 3D, or 4D spectral–spatial imaging.

Overhauser enhanced MRI (OMRI), also known as proton electron double-resonance imaging (PEDRI), is a double-resonance technique of electron and nuclear spins. In brief, the OMRI technique can encode characteristic EPR spectral information on a high-resolution MRI. The method uses paramagnetic contrast agents, saturated by EPR irradiation, to polarize water protons through dynamic nuclear polarization (DNP). The polarized protons enhance the MRI signal intensity. Because Overhauser enhancement is inversely dependent on electron relaxation-rate constant T_{2e}, it can reflect EPR spectral information, which depends on the pO_2 (44).

Among the functional imaging methods, EPR-based modalities have a unique characteristic that the physiologic information can be better detected through EPR spectral information. The *f*MRI techniques using redox-sensitive paramagnetic contrast agents provide another possibility of imaging the physiologic information. EPRI, OMRI, and MRI thus complement each other and together provide co-registered anatomic and functional/physiologic information. In this review, applications of magnetic resonance–based functional imaging techniques (*i.e.*, separation of localized biologic information based on paramagnetic compounds) are summarized.

FUNCTIONAL INFORMATION FROM PARAMAGNETIC PROPERTY

Mouse models of human cancer are widely used for investigation. Functional imaging of mouse models provides important physiologic/pathologic information noninvasively. EPRI with nontoxic paramagnetic spin probes (free radicals) can be used in small-animal models to study tissue pO_2 and tissue redox status. In functional EPRI, in addition to spatial distribution, information such as EPR linewidth or EPR signal decay rate also is obtained. Simple paramagnetic loss can also be detected by T_1-weighted MRI instead of EPRI, based on radical reaction rates independently known from EPR spectroscopy. Quantitative oxygen mapping can be achieved by EPR-related spectroscopic imaging techniques (*i.e.*, CW EPRI, time-domain EPRI, and OMRI) using TAM radicals as an oxygen concentration–sensitive probe. Nitroxyl radicals are used as redox-sensitive probes for dynamic imaging by CW EPRI, OMRI, and T_1-weighted MRI. Several magnetic resonance modalities and their combination with several paramagnetic compounds can be used to obtain useful information for planning radiation therapy in our laboratory (Fig. 1).

Although one important benefit for time-domain EPR is its high temporal resolution, a major limitation for time-domain EPR is that, ideally, only probes with a single narrow EPR line such as TAM radical (linewidth is 0.2 Gauss) can be used as spin probes. CW EPR, conversely, has no limitation on the linewidth or shape of the EPR spectrum of the contrast agent or both. Therefore, CW EPRI can use nitroxyl radicals (linewidth, ~1.4 Gauss). The important advantage of OMRI, conversely, is the high spatial resolution and the additional possibility of slice selection. OMRI also has a linewidth limitation, which is less restrictive than time-domain EPR. Some of the nitroxyl radicals can be adequately used as contrast agents for OMRI. Paramagnetic substances can be indirectly detected by MRI because of the proton T_1-shortening effect with clear anatomic resolution, although it will be difficult to extract quantitative EPR spectral information.

Figure 2 shows the examples of paramagnetic compounds for *in vivo* EPRI, OMRI, and MRI. Nitroxyl radicals (Fig. 2A and B) can be used for redox imaging using CW EPR and OMRI. Nitroxyl radicals can also be used as redox-sensitive contrast

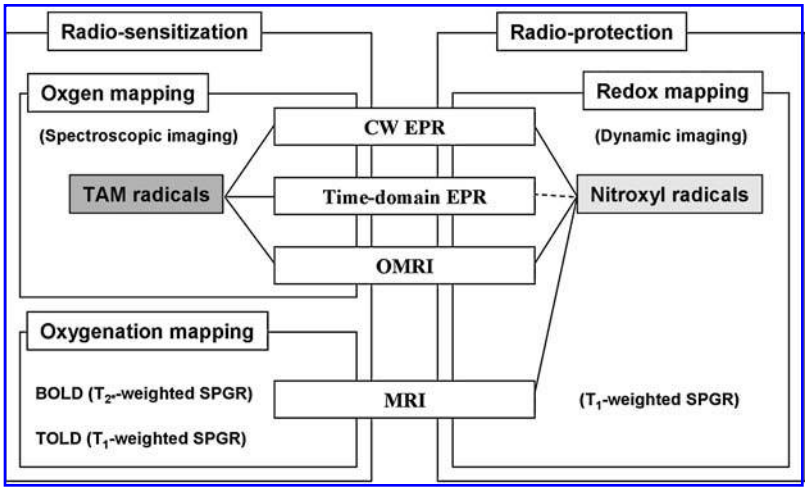

FIG. 1. A schematic illustration of the classification of magnetic resonance–based functional imaging techniques and applications being developed to support radiation therapy. *In vivo* oxygen mapping is related with radiosensitization. Quantitative oxygen mapping can be achieved by EPR-related spectroscopic imaging techniques (*i.e.*, CW EPRI, time-domain EPRI, and OMRI) using TAM radicals as a pO_2-sensitive contrast agent. *In vivo* redox mapping is related to radioprotection. Nitroxyl radicals are used as redox-sensitive contrast agents for dynamic imaging by CW EPRI, OMRI, and T_1-weighted MRI.

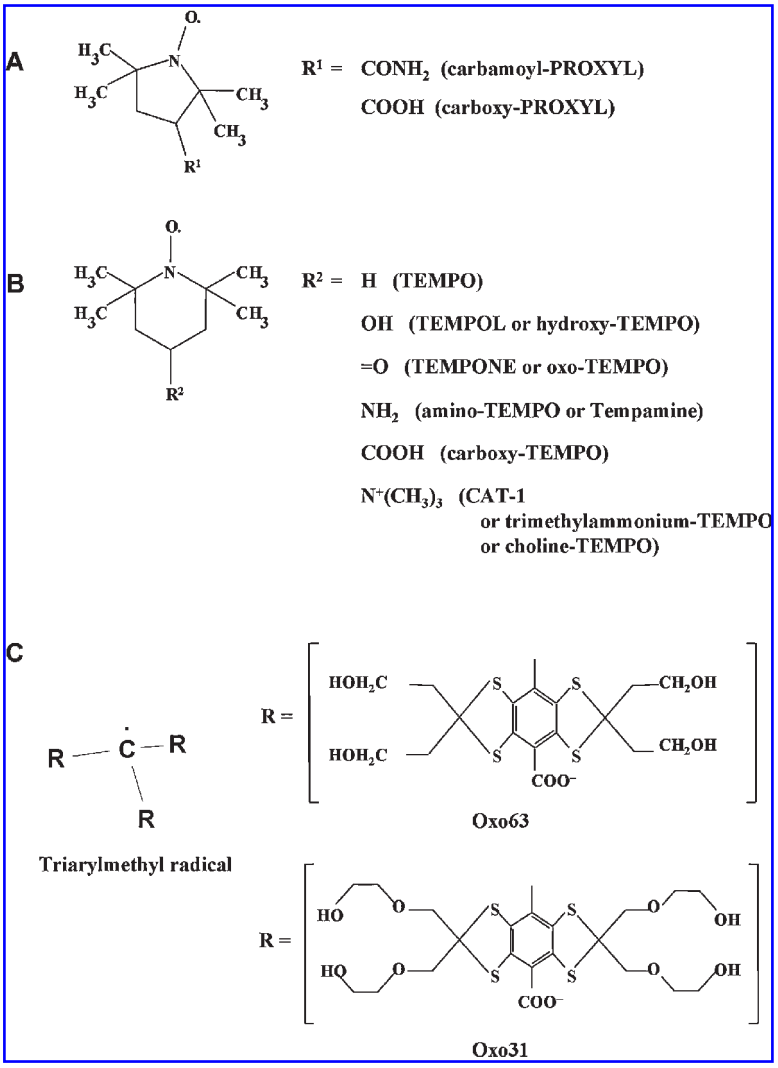

FIG. 2. Examples of nitroxyl spin probes (redox-sensitive contrast agents) and TAM spin probes (oxygen concentration–sensitive contrast agents). (**A**) Five-member rings (PROXYL derivatives). (**B**) Six-member rings (TEMPO derivatives). Water solubility and chemical reactivity depends on the molecular structure. (**C**) Oxo63 and Oxo31 are low-toxic, water-soluble molecules with carbon-centered radicals, which have a single EPR line.

agents for T_1-weighted MRI. Unfortunately, nitroxyl radicals are unsuitable for time-domain EPR because of their broad linewidth. Less-toxic TAM derivatives (Fig. 2C), such as Oxo31 and Oxo63, are well suited for *in vivo* time-domain EPR and OMRI because of their narrow linewidth and high solubility in water. Particulate paramagnetic probes, such as India ink (25), glucose char (109), lithium phthalocynaine crystals (40, 57), have also been proposed for *in vivo* EPR oximetry and imaging in CW modality. These probes give a single-line EPR spectrum whose linewidth depends on the *in vivo* oxygen concentration.

EPR-related spectroscopic imaging techniques can separate pixel-wise EPR spectral information from the spatial data. Such spectroscopic imaging leads to EPR oximetry, which is based, for example, on the EPR linewidth measurement of TAM radicals. Tissue pO_2 mapping is based on the pixel-wise spectral information. Dynamic (time-course) imaging techniques, based on mapping the redox-sensitive nitroxyl contrast agent, can be used in the tissue redox status estimation. The pixel-wise decay rate of EPRI, OMRI, or T_1-weighted MRI intensity can provide tissue redox mapping.

CONVENTIONAL CW EPRI

The CW EPRI method is basically similar to the first NMR imaging developed by Lauterbur in 1973 (53), except that a relatively larger magnetic field gradient is required for the CW EPRI. The initial EPRI technique was developed in a field of material sciences in 1979. Karthe and Wehrsdorfer (42) showed the possibility of EPR imaging using a pair of field gradient coils. Two particles of DPPH at a distance of 200 μm were separated on an EPR spectrum. The first 2D EPRI was reported by Hoch and Day (36). An EPR image of two diamonds, which have a paramagnetic defect in the crystal, was reconstructed on a 20 $\times$ 20 matrix by algebraic reconstruction technique (ART) from 12 projections oriented every 15 degrees in the range from 0 to 180 degrees. To obtain pure spatial distribution of the paramagnetic center in the sample, a spectral deconvolution technique was introduced (35, 85, 86). In the late 1980s, the application of the EPRI branched into two areas, which were microscopic imaging (37, 38, 78, 87) and *in vivo* imaging. The first L-band EPRI was reported by Berliner and Fujii in 1985 (10). One-dimensional EPR spectra of a nitroxyl radical, TEM-

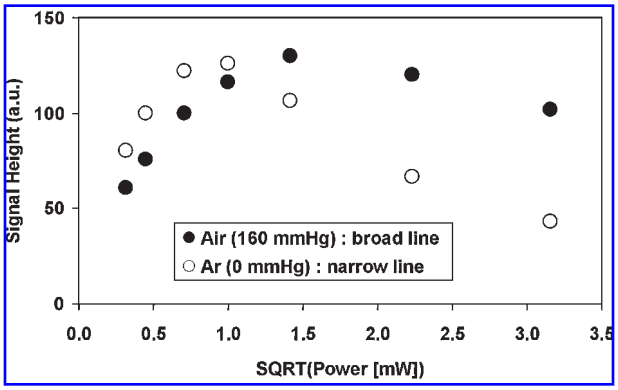

FIG. 3. Relation between the microwave power and EPR signal height of 2 m*M* Oxo63 aqueous solutions at different oxygen concentrations. Solid and open circles indicate values from the air-equilibrated (pO_2, 160 mm) and argon-equilibrated (pO_2, 0 mm) samples, respectively. The argon-equilibrated sample (*i.e.,* narrow linewidth condition) was power-saturated more easily.

POL, absorbed into a celery stem were obtained under 24.3 Gauss/cm of the field gradient. The first 2D *in vivo* EPRI of a tumor grown on a living mouse tail was reported by Berliner *et al*. in 1987 (11). After that, 2D or 3D EPRI studies in mice or rats were reported from several groups (2, 4, 41, 103). A variety of EPRI systems and equipment for biologic samples were developed by each group for their experimental purpose (3, 13–15, 24, 29, 47, 82, 83, 95).

The projection reconstruction (backprojection) technique used in the EPRI was developed in the field of radiographic tomography, such as CT, positron emission tomography (PET), single-photon emission computed tomography (SPECT), *etc*. The backprojection algorithm can manipulate values that can be integrated, such as radiation counts. The electron spin density is the analog of radiation count in the case of the EPRI. An EPR spectrum obtained under a field gradient can be used as projection data for the image, when the EPR spectrum consists of a single line. In the case of a system with a hyperfine multiplet, one can obtain the projection information from any individual hyperfine line, as long as the features from other hyperfine lines are far away and do not overlap. If the features overlap, algorithms are available to remove this interference (45). After suitable filtering of the projection data (the EPR spectrum under the field gradient), the intensity of each data point on the projection can be directly backprojected to obtain the image matrix (filtered backprojection, FBP). Theoretically, the electron spin density is proportional to the doubly integrated EPR spectrum (area of the integrated spectrum). An identical spin density results in an identical area of the integrated spectrum. If the EPR linewidth is narrow and a constant, this filtered backprojection process can give a true density mapping. However, the linewidth of the EPR spectrum depends on the microenvironments of the electron spins. A large linewidth makes the EPR signal height small, and a small linewidth makes the EPR signal height large. In other words, a broad linewidth makes the spatial distribution blurred because of the wide distribution of the values. However, this fact suggests that the EPRI can readily reflect spectral information as its image intensity.

The first trial of a functional EPRI was done by Swartz and his colleagues (9). They obtained 2D EPRI showing an intensity difference depending on the tissue (*i.e*., fat and muscle) (9). This is due to the oxygen solubility in lipid-rich and water-rich environments. They also showed EPRI intensity variations between fat and muscle depending on the oxygen concentration in the perfused gas. The variation of EPRI intensity based on an effect of EPR linewidth on the microwave power saturation was reported (8, 16). This intensity variation was made by a change in the microwave power saturation behavior of a dif-

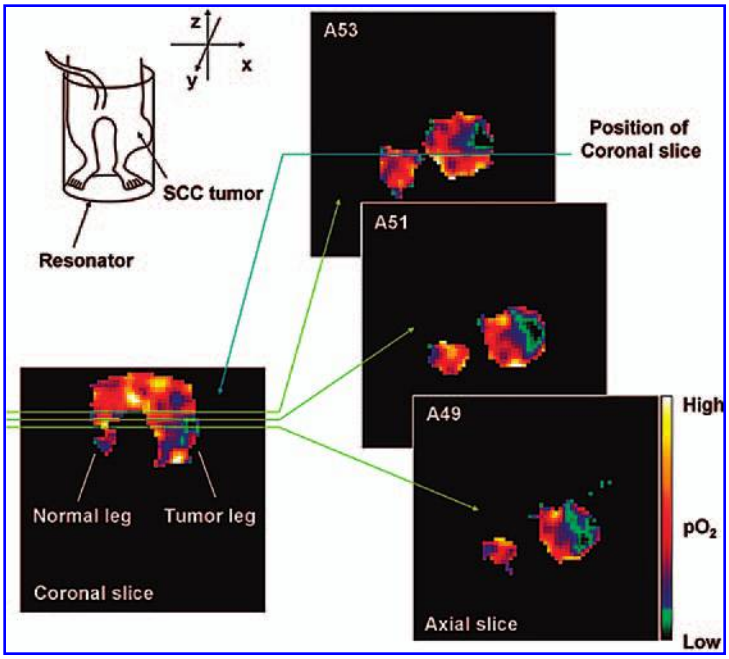

FIG. 4. An example of 3D oxygen mapping obtained by the CW EPRI high- and low-power method. This method is based on the electron T_{1e} difference caused by oxygen concentration in the sample. The insert in the upper left indicates positioning of the mouse with an SCC tumor on its right leg in a Litz coil–type resonator. A hypoxic core can be found in the center of the tumor.

ferent EPR linewidth, which is due to variable oxygen concentration in the samples.

Recently, we tried to obtain quantitative oxygen mapping based on microwave power saturation, which depends on T_{1e} (T_1 relaxation of electron spin) (33). The microwave power saturation easily occurs for a spin probe having a narrower EPR linewidth due to longer T_{1e} relaxation time. However, a spin probe with broad EPR linewidth is resistant to microwave saturation, because of short T_{1e} relaxation time. Similarly, for an individual free radical species, a narrower linewidth in a hypoxic environment can be saturated more easily than the broader linewidth in an oxygenated environment (Fig. 3). Theoretically, the EPR signal intensity increases linearly, depending on the root of the microwave power in nonsaturating conditions. When microwave saturation occurs at a higher microwave power, the EPR signal intensity becomes lower than the predicted intensity. With the EPR signal or EPR image intensities obtained at two different microwave power levels, the original linewidth of the paramagnetic probe is predictable. The advantage of this method is a relatively short data-acquisition time. Because just two images obtained at different power levels can make an oxygen mapping possible, the data-acquisition time will be just a double of the usual imaging condition. The resolution of the image is not identical throughout the image matrix, because the EPR image resolution depends on the linewidth of the paramagnetic probe. The two images taken at different power levels may have different image resolutions. This effect is small when a suitable spin probe is used. A triarylmethyl radical, such as Oxo63 (Fig. 2C), which has very narrow EPR linewidth and relatively lower sensitivity to the oxygen concentration in the sample (0.19 Gauss at $pO_2 = 0$ mm Hg to 0.24 Gauss at $pO_2 =$ 160 mm Hg) may be good to use for this T_{1e}-based oximetry method. With Oxo63 as the spin probe continuously administered *via* a tail vein, a 3D oxygen mapping in an SCC tumor implanted in the hind leg of a mouse was obtained (Fig. 4). By an additional measurement with different a parameter, which was the microwave power in this case, an additional dimension (*i.e*., spectral information) could be encoded in the CW EPR image.

Another functional imaging modality is dynamic (time-course) imaging. In this case, the additional dimension is time. After the rapid development of computer systems, rapid instrumental control and data manipulation has been possible. A rapid succession of measurement of conventional 2D EPR images of an administered nitroxyl radical in an experimental animal can provide the time course of clearance of nitroxyl radical. The assumption that all locations in the sample must give a single EPR spectral component is again valid in this conventional modality. Such measurements allow tissue (normal or tumor)-dependent reduction rate constants of the nitroxyl radical to be calculated pixel-wise from a time-series of EPR images (Fig. 5). Figure 6 shows an example of *in vivo* EPR redox mappings showing a different decay rate of a nitroxyl radical in tumor tissues treated or untreated with a GSH inhibitor (52).

The earliest *in vivo* EPR image of tumor on a mouse tail required 32 min for data acquisition of four projections in 1987 (11). In 1994, Alecci *et al*. (4) showed two sequential 2D EPR images of coronal plane of rat abdomen after administration of carboxy-PROXYL. In that time, one image data set still required 5 min for acquisition of eight projections. Trials of the *in vivo* dynamic EPR imaging (*i.e*. time-course, time-resolved, or temporal imaging) have been reported from 1996 by several groups. Time-courses of 3D EPR images of isolated rat heart (49), living rat head (108), and 2D images of living mouse heart and bladder (43) were reported using nitroxyl contrast agents. However, those 3D images required relatively long acquisition times (for example, 11 min for 10×10 projections and 3 min for 9×9 projections, respectively). Recent notable reports use series of 2D EPR images to obtain a redox mapping. Different clearances of i.v.-injected nitroxyl radical (carbamoyl-PROXYL) in normal and RIF-1 tumor tissues of mice were exhibited by series of 2D EPRI measured at the L-band (51). The clearance of nitorxyl radical was faster in the tumor tissue than in the normal tissue. They also showed a difference of decay rate of carbamoyl-PROXYL in an RIF-1 tumor of BSO (GSH inhibitor) treated and nontreated mice (52). Figure 6 shows their results of BSO treatment/nontreatment. The decay rate of nitroxyl radical was GSH dependent. Different clearances of carbamoyl-PROXYL in the RIF-1 tumor of control and carbogen (gas mixture of 95% O_2 and 5% CO_2) breathing mice were obtained (39). The decay rate of the nitroxyl radical was decreased by oxygenation of tumor tissue. At the same time, the validity of EPR redox mapping was estimated by the different decay

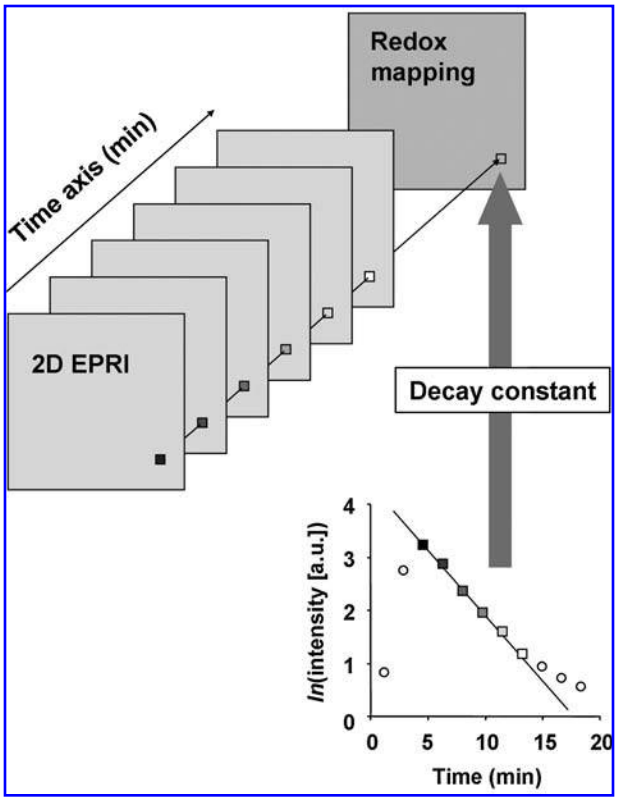

FIG. 5. A schematic drawing of the concept of dynamic imaging. The additional time dimension to the spatial mapping of the paramagnetic contrast agent and functional information, such as pharmacokinetics of the contrast agent, can be tagged on to the EPR image. The time axis is by sequential measurement of several EPR images. Consequently, pixel-wise decay rates of EPR image intensity can be obtained.

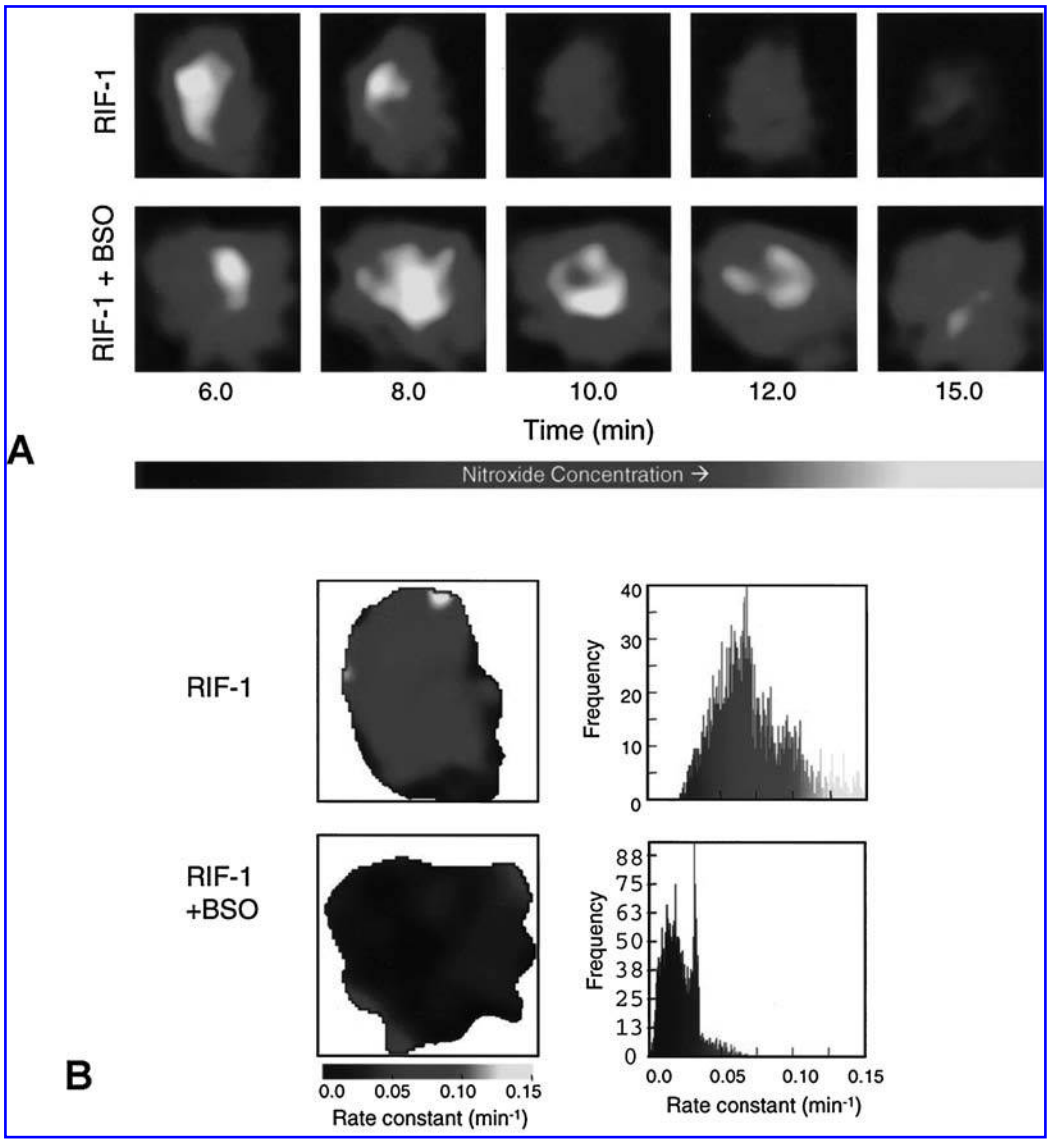

FIG. 6. An *in vivo* EPR redox mapping (52). (**A**) Clearance of carbamoyl-PROXYL in RIF-1 tumor tissue after tail-vein infusion. 2D images of the nitroxide from tumor (untreated and BSO-treated) were measured using L-band EPRI. The image data were acquired using a magnetic field gradient of 15 G/cm at 16 orientations. The nitroxide in the tumor of the BSO-treated mouse persisted longer, compared with that in the untreated mouse. (**B**) Redox mapping of tumor. Two-dimensional spatial mapping of pseudo–first-order rate constants (*left panels*) and frequency plot (*right panels*) of the nitroxide reduction-rate constants in the RIF-1 tumors of untreated and BSO-treated mice were obtained from the time-course image data shown in (**A**).

rate of TEMPOL in a four-tube phantom containing a different flux of superoxide generation (106). The faster decay rate of carbamoyl-RROXYL in an SCC tumor has been monitored by EPRI (75, 101). Different decay rates of a nitroxyl radical in different regions of a mouse brain have been reported (93).

Recently, a novel data-acquisition method for the conventional CW EPRI using spinning field gradient was proposed (88) and applied to low-frequency EPRI (17). Figure 7 shows a comparison of a data-acquisition sequence of the conventional EPRI and the spinning field-gradient method. The data acquisition during a spinning field gradient gives a vertical data column, and then a simultaneous field sweep shifts the column. The low impedance of the field gradient coil makes possible the rapid spinning of field gradient (10–60 Hz in the X-band experiment, 3–24 Hz in the 300-MHz experiment). The field sweep was done only once within a few seconds. Therefore, a 2D EPRI data set can be obtained within a few seconds. Such a fast EPRI technique may give a new concept of molecular functional EPRI in the future.

MR REDOX IMAGING

Spatial resolution of an EPR image is not sufficient to distinguish the particular organ/tissue, for the following reasons: (a)

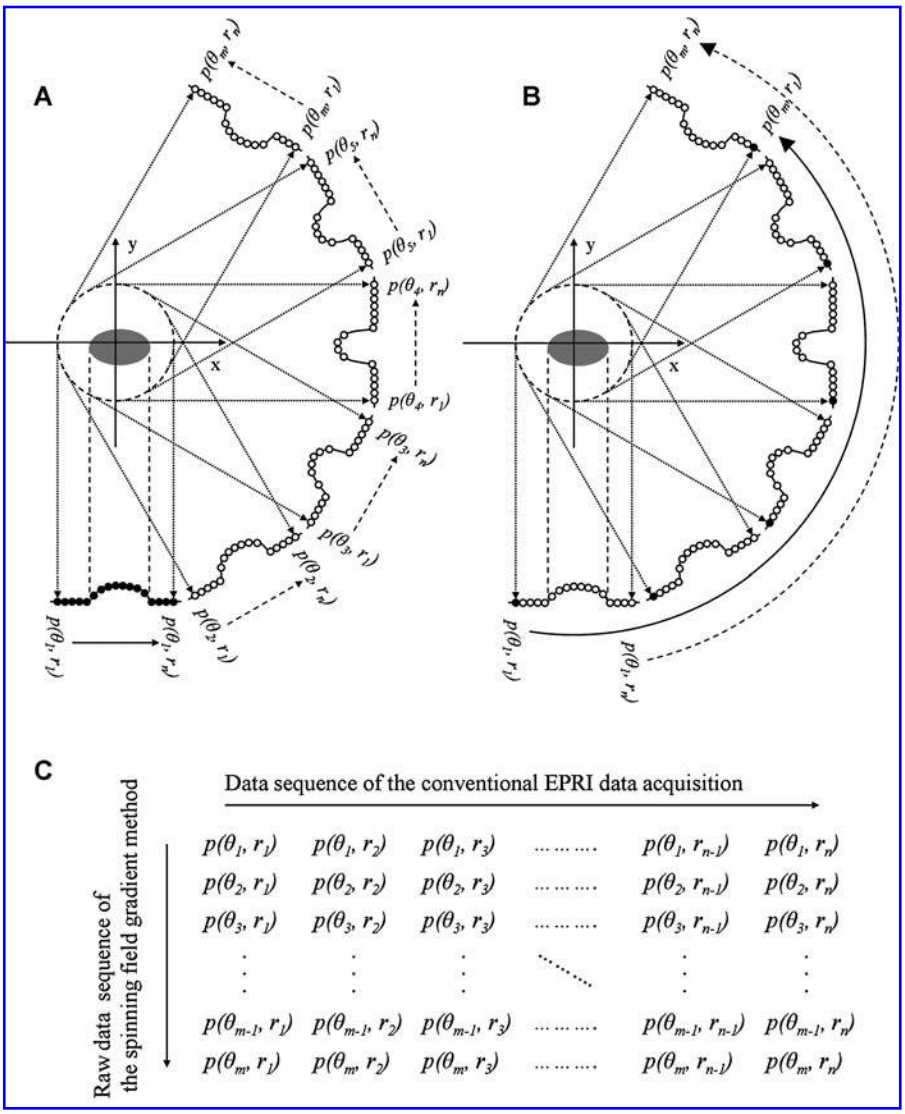

FIG. 7. Comparison of the conventional EPRI data acquisition and the spinning field-gradient method. (**A**) Conventional EPRI data acquisition. The direction of magnetic field gradient, θ, is fixed during a magnetic field sweep. The magnetic field, r, is incremented to obtain a projection consisting of n data points. After reversing the magnetic field sweep, the projection data are obtained for the next direction. (**B**) Data acquisition by the spinning field-gradient method. The direction of magnetic field gradient was spinning continuously. The increment of θ (*i.e.*, number of projections, m) depends on the frequency of data acquisition. The magnetic field, r, is incremented in n-steps to obtain n data points on each projection. (**C**), Data matrix of 2D EPRI. Both methods give the same data matrix. In conventional EPRI, projection data are obtained with a fixed-angle θ with changing magnetic field r, and then the data matrix is filled row by row. In the spinning-gradient modality, a fixed magnetic field r with changing angle θ gives a pseudo spectrum, and the data matrix is filled column by column.

the relatively broad EPR linewidth of the nitroxyl contrast agent blurs the true distribution, and (b) EPR can detect only the distribution of the nitroxyl contrast agent, but no anatomic information is observed. In addition, the 2D EPR image is not an individual slice, as in MRI and OMRI, and all information from the vertical direction to the 2D plane overlaps. Although the 3D EPRI has an advantage to obtain slices, 3D EPRI acquisition required a relatively long acquisition time and is not suitable to obtain good temporal resolution. Therefore, most cases of the notable EPR redox imaging consist of obtaining a time sequence of the 2D EPR images instead of 3D EPR images.

The nitroxyl radicals in an aqueous sample can be also detected by MRI through enhanced T_1-weighted contrast because of its proton T_1-shortening effect. T_1-weighted gradient echo MRI can provide an *in vivo* redox mapping based on the reduction of the nitroxyl radical with finer spatial resolution and temporal resolution compared with CW EPRI (75). When it is validated that the *in vivo* paramagnetic loss of the nitroxyl radical used in the experiment was caused by only simple one-electron reduction to the corresponding hydroxylamine, T_1-weighted gradient echo MRI is better suited to see the tissue/organ-dependent redox status. However, detection of the nitroxyl radical by MRI is based on T_1-weighted signal change, which requires an image obtained before administration of the nitroxyl contrast agent as a baseline. Hence, the MRI can only detect contrast differences before and after the challenge by the nitroxyl contrast agent, requiring the administration of the nitroxyl contrast agent between the sequences of image acquisition. Conversely, in EPRI and OMRI, the concentration of the nitroxyl radicals can be assessed directly.

EPR SPECTRAL–SPATIAL IMAGING

Projection reconstruction spectral–spatial imaging (PRSSI) in CW EPR

A static field gradient imparts spatial information onto an EPR spectrum in which the spectral information (linewidth) and

spatial information are superposed. The variation of directions of the static magnetic field gradient can expand the spatial dimension to 2D or 3D. As mentioned earlier, spectral information still exists on the raw 2D or 3D EPRI data. A variation of the magnitudes of field gradients can expand the spatial dimension of EPRI to give a spectral–spatial pseudo matrix. Figure 8 indicates a schematic drawing of theory of CW EPR spectral–spatial data acquisition. The relative magnitudes of field gradient and sweep width define the pseudo viewing angle in the spectral–spatial space. The relation between the pseudo angle α (degree) and amplitude of field gradient G_α (Gauss/cm) is given by

$$G_\alpha = \tan\alpha \times \Delta H/\Delta L, \quad (1)$$

where ΔH (Gauss) and ΔL (cm) are spectral and spatial window width of the spectral–spatial pseudo matrix. Because tan α approaches infinity as the angle α approaches to ± 90 degrees, the maximum pseudo angle $\pm\alpha_{max}$ is limited by the instrumentally possible maximal field gradient. Data will be missing for viewing angles from $\pm\alpha_{max}$ to ± 90 degrees, known as

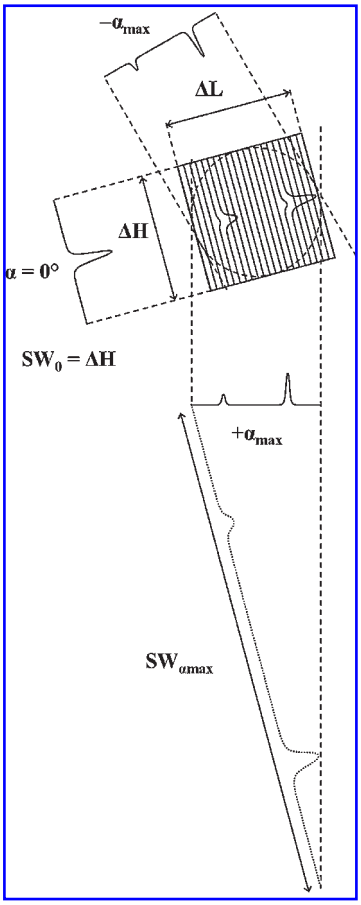

FIG. 8. The theory of CW EPR spectral–spatial imaging data acquisition. A 2D spectral–spatial pseudo plane consisted of a spatial window ΔL, and spectral window ΔH is seen from the maximum angle α_{max}. The projection profile of α_{max} obtained under $G_{\alpha max}$ requires $SW_{\alpha max}$. Finally, all projections are interpolated to identical data points.

the "missing angle." The sweep width SW_α corresponding to a viewing angle α is given by,

$$SW_\alpha = \Delta H / \cos\alpha. \quad (2)$$

All projections are interpolated to identical number of data points to be subjected to projection-reconstruction process, such as FBP or ART. Using a suitable variation of directions and amplitudes of magnetic field gradients, 2D, 3D, and 4D EPR spectral–spatial images can be reconstructed by conventional projection-reconstruction algorithms.

The projection-reconstruction modality of the EPR spectral–spatial imaging method is basically similar to the NMR spectral–spatial imaging (12, 54, 97). The theory of EPR spectral–spatial image-reconstruction algorithms were first described by Maltempo (64). Individually, Ewert and Herrling (23) first applied Lauterbur's method to EPR and obtain a 2D EPR spectral–spatial image. Later, the basic principles of EPR spectral–spatial image-reconstruction technique were developed by Maltempo *et al*. (65, 66). Applications of the EPR spectral–spatial imaging technique were developed also for material sciences at X-band (67, 89, 96). 3D spectral–spatial (one spectral and two spatial dimensions) images of a phantom containing six different species were carried out and compared by CW and time-domain (electron spin echo) EPR at X-band (102).

The basis of EPR oximetry is the measurement of the EPR linewidth of a paramagnetic probe in a sample/animal. Therefore, direct measurement of the EPR linewidth from spatially resolved EPR spectra in an *in vivo* EPR spectral–spatial image provides tissue pO_2 mapping capability noninvasively. Kuppusamy *et al*. (46) developed a 3D EPR spectral–spatial imaging system at 1.3 GHz for isolated rat heart and rabbit aorta using TEMPO as the oxygen probe. They successfully obtained a 4D EPR spectral–spatial image of phantoms and an isolated rat heart using ^{15}N-d_{16}-TEMPONE as the oxygen probe (48). Halpern *et al.* (30) also proposed *in vivo* oximetric imaging in deep tissue using an EPR spectral–spatial imaging technique. Halpern *et al.* (31) carried out EPR spectral–spatial imaging of the abdominal part of a whole mouse using several nitroxyl radicals as the oxygen probe.

Combination of the EPR spectral–spatial imaging technique and a suitable paramagnetic probe, which is stable and has a simple EPR spectrum, allowed 3D imaging of the oxygenation in the gastrointestinal tract in living mice (34). A 2D pO_2 mapping in a mouse tail was reported with a nitroxyl contrast agent, carbamoyl-PROXYL (94). However, the nitroxyl contrast agents were unstable in the living system to sustain the EPR signal intensity long enough to perform oximetry. The lack of an ideal paramagnetic probe for oximetric imaging had been mentioned (50). Useful paramagnetic probes for EPR oxygen mapping should possess the following characteristics: (a) simple EPR spectrum; (b) oxygen-dependent linewidth; (c) water solubility; (d) chemical and biologic stability; and (e) low toxicity. Several TAM radicals have been developed as contrast agents intended for OMRI oximetric imaging (7, 105). Finally, Oxo63 and/or Oxo31 (Fig. 3), which satisfy these requirements, were developed by Nycomed Innovation (Malmö, Sweden). Several spectral–spatial EPRI experiments were reported with Oxo63 or Oxo31 (21, 70).

In a different context, the EPR spectral–spatial imaging tech-

nique was used to separate multiple free radical species in a single experimental system. Matsumoto and Utsumi (69) proposed a simple method to separate 2D distribution of multiple free radical species using a phantom containing two nitroxyl contrast agents, carbamoyl-PROXYL and PTIO. With this method, 2D distributions of hydroxyl radical trapped by DMPO (DMPO-OH) and nitric oxide trapped by Fe^{2+}-MGD (Fe^{2+}-MGD-NO) in a phantom were successfully separated. The same method was applied to observe the fates of highly concentrated (300 m*M*) CAT-1 solution encapsulated in liposomes and a free 2 m*M* CAT-1 solution injected in mice (72). The location of anthralin radical caused in mouse skin by UV-A irradiation was calculated from the location of DPPH radical as a landmark in a microscopic 2D EPR spectral–spatial image at X-band (73). The unique characteristic of CW EPR PRSSI is that the multiple paramagnetic species can be detected simultaneously.

Time-domain EPR imaging

Time-domain EPR is also referred as Fourier transformation (FT) EPR. The time-domain EPR technique is severely limited by the very fast electron-relaxation process. Hence the paramagnetic species suited to the time-domain EPR measurement should have quite a narrow EPR linewidth. EPR spin-echo imaging techniques were developed by Eaton and colleagues almost simultaneously with CW EPR spectral–spatial imaging at X-band (19, 20). In 1990, 3D spectral–spatial imaging techniques were achieved by both the electron spin echo and the CW detections at X-band (102). With the availability of TAM radicals, *in vivo* application of the time-domain EPR was implemented in 1997 (80), nearly 10 years later than the first *in vivo* CW EPR imaging. The initial developments of low-frequency (radiofrequency) time-domain EPRI were carried out by two groups [*i.e.*, Sotgiu and colleagues (6, 91, 92) and Krishna and colleagues (1, 18, 98)]. Both groups used detection of free induction decay (FID) rather than spin echo. The imaging method was based on the projection reconstruction with a combination of field gradients applied on polar coordinates.

The first example of physiologic imaging obtained by time-domain EPRI was reported by Subramanian *et al.* (99) with T_{2e}^* (T_2^* relaxation of electron spin)-based EPR oxygen mapping. When several absorption spectra were obtained from one FID with progressively increasing acquisition delay, the peak height of the absorption spectra decayed as an exponential function of the delay from the initial time. This decay of the peak height is based on T_{2e}^*. Therefore, comparison of several 2D or 3D spatial images reconstructed from projection data sets of several starting times gives T_{2e}^*-based oximetric information. The FID-based imaging and oximetry is fraught with artifacts because at high gradients, the T_{2e}^* becomes short because of increased frequency band-width and interference, leading to considerable loss of net signal within the "dead-time" of the spectrometer. In oblong systems, the integrated intensities of projections do not remain constant throughout all gradient directions, not to mention the distortion at the edges from the linewidth of the probe, although this can be removed by standard deconvolution methods. In summary, the FID-based FBP EPR imaging method does not work well except with probes having a very long relaxation time.

Krishna and colleagues have continued developing the 300-MHz time-domain EPRI instrument and imaging modalities to achieve a reliable and reproducible noninvasive *in vivo* EPR pO2 mapping method. The performance of the time-domain EPR spectrometer/imager was described elsewhere with detailed comparison with our 300-MHz CW EPRI instrument (107). An alternative spatial encoding scheme, the single-point imaging (SPI) modality, was developed for time-domain EPRI and practically eliminates the linewidth effects and dead-time effects (100). The method also can be extended to provide a time-domain EPR spectral–spatial imaging modality. The SPI, which is also referred to as constant-time imaging (CTI), was first introduced to NMR imaging in solids (22, 68). Although the details of principles of time-domain EPR SPI have been described elsewhere (100, 101), an outline of the modality is summarized in Fig. 9.

As shown in Fig. 10, a series of single point images can be obtained from every time point of the FID. Those image intensities decrease with time τ_p depending on the transverse re-

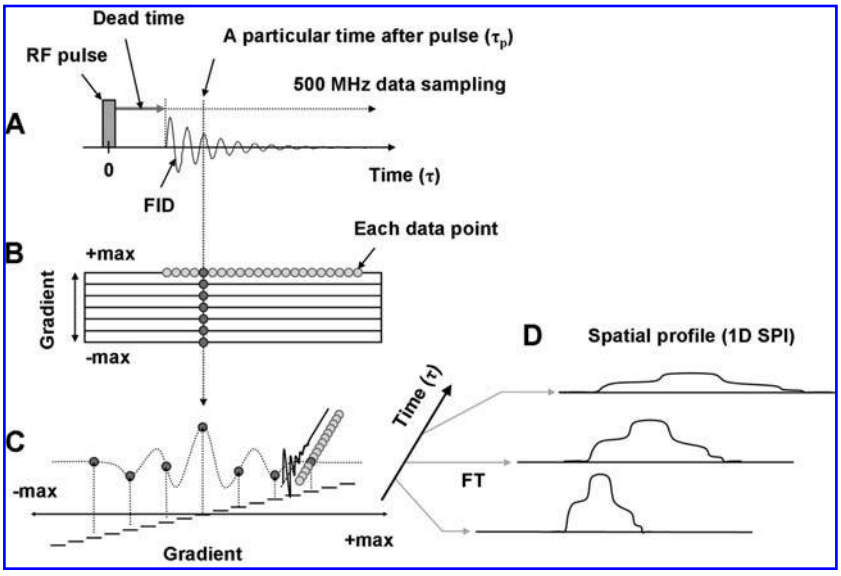

FIG. 9. Schematics of single-point imaging. (**A**) The FID after excitation pulse is digitized using a fast ADC (500 mega samples/s). (**B**) The gradients are systematically incremented from a negative maximum to a positive maximum. (**C**) The phase imparted on any particular time point, τ_p, of the set of FID simulates a gradient-echo response in the transverse magnetization. A set of FID data was saved for FT image reconstruction. Each time point of the FID set contains the full image information. (**D**) A series of 1D spatial profiles (*i.e.*, 1D SPIs) was obtained by FT of data points at each time point. The FOV of SPIs were varied depending on the time after the pulse, τ_p.

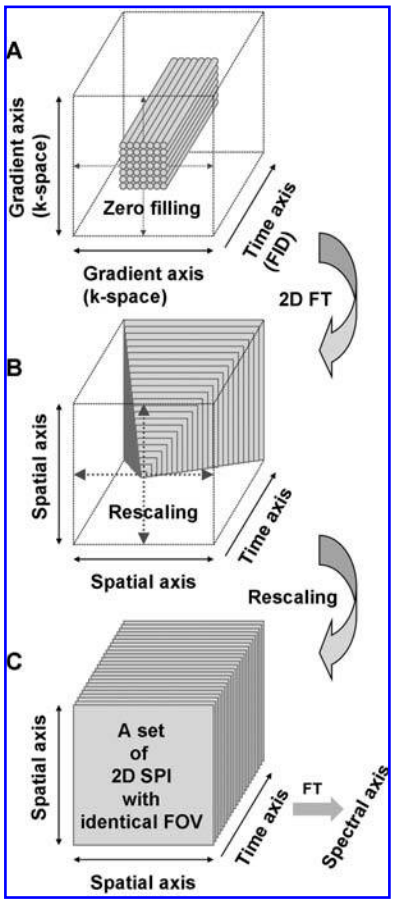

FIG. 10. Schematic procedure for 2D SPI reconstruction. (**A**) A set of FIDs measured under 2D field gradient was placed on a k-space, and then the matrix was zero filled ($2^n \times 2^n$) for FT. (**B**) Although 2D FT procedure for each time point gives a set of 2D SPI, delayed time points represent larger durations of the phase-encoding gradients and lead to lower Nyquist bandwidths corresponding to smaller FOVs (*i.e.*, "zoomed-in" images). Gray slices in **B** indicate regions of identical FOV for each time point. (**C**) All SPIs were rescaled to an identical FOV, and a 3D matrix (2D spatial and 1D time domain) was obtained. Finally, time axis can be transferred to spectral axis by FT.

laxation, although individual images have no linewidth information. Hence the spatially separated FID information (*i.e.*, spectral information) can be reconstructed on the time axis. Therefore, the EPR SPI method is neither more nor less than EPR spectral–spatial image reconstruction in a Fourier k-space. However, the field of view (FOV) of a single point image depends on the delay τ_p time after the pulse and is given by

$$\mathrm{FOV} = \mathrm{N} \cdot 2\pi / (\gamma_e \cdot \tau_p \cdot \mathrm{G_{max}}) = 2\pi / (\gamma_e \cdot \tau_p \cdot \Delta\mathrm{G}) \quad (3)$$

where N is the number of samples in k-space, γ_e is the gyromagnetic ratio of the electron, G_{max} is the maximum field gradient and ΔG is the incremental step of field gradient. Images generated from different time points in the FID should be rescaled to an identical FOV for a direct pixel-by-pixel comparison. Finally, T_{2e}^* relaxation time for each pixel was estimated from the reconstructed decay curve. In addition, a 2D spectral–spatial image can be obtained by FT of time axis. The method was called as FT constant-time spectral–spatial imaging (FT-CTSSI). Using a combination of 2D or 3D field gradients, 3D or 4D spectral–spatial imaging can be obtained. Figure 10 is a schematic drawing of the procedure for 3D FT-CTSSI reconstruction.

This procedure should give a reliable estimate of transverse relaxation times and apparent linewidths in principle. However, small errors in resizing the images could manifest as serious edge artifacts in practice. The gradient increment step ΔG and the time after pulse τ_p determine the analytic image resolution given by FOV/N. An object in the SPI constructed from very short delay time τ_p, which corresponds to very low resolution, must have a blurred edge because of "brute-force" interpolation. Such erroneous values from the edge lead to errors in the estimate of the transverse decay constant, and hence linewidth. Therefore, the spatial resolution of SPIs belonging to time axis should be identical to obtain reliable pixel-wise transverse decay constants.

Several SPI data sets with multiple G_{max} can be combined to provide identical resolution with different τ_p (32). A large gradient step ΔG gives a small FOV at short τ. Conversely, small ΔG gives the same FOV at long τ. Several SPIs of the same FOV can be picked up from multiple G_{max} data sets. The combined data set form multiple G_{max} data sets to provide uniform resolution and FOV leads to more reliable quantification of T_{2e}^* (Fig. 11). Using the multiple G_{max} method, the oxygen concentration in a phantom containing 0–40 mm Hg oxygen was estimated with accuracy of ± 0.9 mm Hg (74). The result of *in vivo* 3D oxygen mapping (4D CTSSI) showed the presence of a hypoxic core in the SCC tumor implanted in the right hind leg of a C3H mouse (Fig. 12). A 3D image with $25 \times 25 \times 25$ (= 15,625 gradient steps) can be done within 3 min with an average of 2,000 FIDs, whereas a 2D image with similar gradient steps can be accomplished in <15 s.

Halpern and colleagues (63) developed a spectral–spatial EPRI using electron spin-echo detection at 250 MHz, and reported oxygen-concentration mapping in phantoms (63). The spin-echo imaging can give information based on T_{2e} instead of the CTSSI, which uses T_{2e}^*, which depends on the field gradient itself. A major advantage of spin-echo detection is that no dead-time problems occur. Hence, FT of echo gives an undistorted spectral shape, and projection-reconstruction process can be well worked on the echo imaging data. Therefore, with an assumption that the EPR spectral shape of the paramagnetic probe is lorentzian, the numbers of data required for 3D spectral–spatial imaging by spin echo is $N_P \times M_E$, where N_P is the number of projection and M_E is the number of echo. The M_E can be much smaller than N_P. However, the 3D CTSSI requires $N^2 \times M_G$, where M_G is a number of G_{max} data sets. Similarly, 4D spectral–spatial imaging by spin echo is available with $N_P^2 \times M_E$ projections (4D CTSSI requires $N^3 \times M_G$). In addition, larger field-gradient strength, which can give better image resolution, can be used. Moreover, it may be possible to use relatively broad linewidth species, such as nitroxyl radicals, to perform imaging.

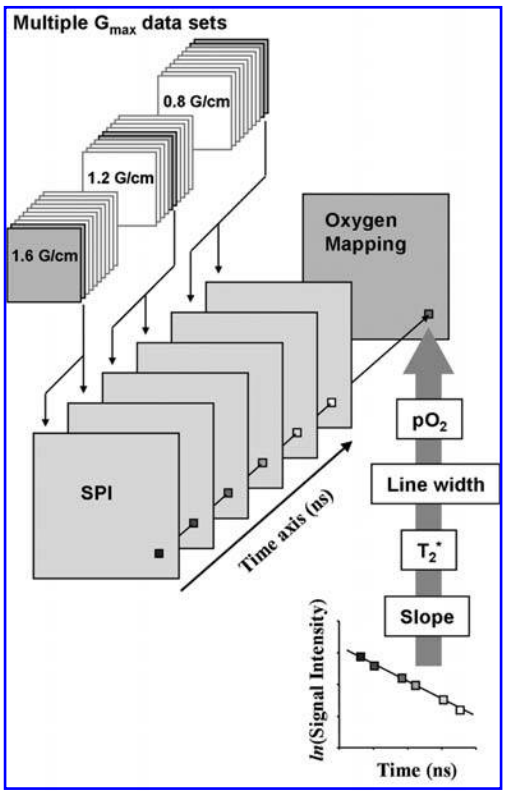

FIG. 11. Estimation of pixel-wise pO_2 from SPI data sets. An SPI data set was reassembled from several SPI data sets obtained using multiple G_{max} settings. Pixels of reconstructed FID are replotted, semilogarithmically. The slope of semilogarithmic plot of FID gives T_{2e}^*. The EPR linewidth can be calculated from the T_{2e}^*. The pO_2 value can be obtained from EPR linewidth using a calibration curve. Finally, pO_2 values are rearranged onto an image matrix.

Comparison of PRSSI and CTSSI in CW EPR

The CTSSI technique can be extended to the CW EPR modality (70). The only difference is that the CW EPR spectrum is in the frequency domain, which can be converted into the time domain by an inverse Fourier transformation and then be treated in the same manner. Both derivative (original) and integral CW spectra could be used for CTSSI reconstruction. Pseudo sampling time $\Delta\tau$ for Fourier-transformed CW data is obtained with the following equation:

$$\Delta\tau = h/(g \cdot \beta \cdot H) \quad (4)$$

where g is g-value, β is the Bohr magneton, h is the Planck constant, and H is the sweep width. Finally, a spectral–spatial image can be observed by the FT of the time dimension. This final spectral–spatial image obtained by the CTSSI should be the same one obtained by the PRSSI when images of both modalities were compared with the same FOV. Table 1 shows a comparison of PRSSI and CTSSI modalities in CW EPR.

If an infinite number of G_{max} data sets can be available, the method can reconstruct undistorted line shapes, although the long data-acquisition time will be impractical even for the FT-CTSSI worked on the time-domain EPRI. Therefore, the three to four G_{max} data sets for T_{2e}^* estimation used in the FT-CTSSI may be valid when a paramagnetic contrast agent having a single lorentzian line EPR spectrum is used. The CTSSI modality in CW EPR may usually work with single G_{max} data because of the long data-acquisition time of the CW modality. Although an advantage of the CTSSI modality for CW EPR is better recovery of spectral shapes, linewidth broadening and background distortion occurred in the single G_{max} data because of the unavoidable variation of the FOV.

Although the CTSSI modality does not have the concept of "missing angle," *per se*, some artifacts observed in the spectral–spatial image obtained by CTSSI look similar to the "missing angle"–based artifact in the PRSSI. Just as infinite or very large gradients cannot be practical (for viewing angle close to

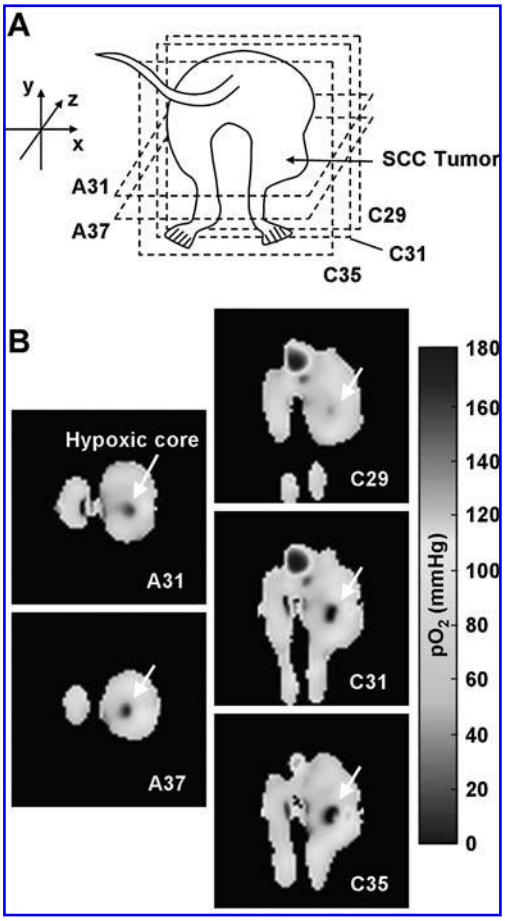

FIG. 12. *In vivo* 3D oxygen mapping by FT-CTSSI. (**A**) Schematics of the geometry of the animal and the slices. The EPRI data sets were obtained with three different G_{max} settings (1.5, 1.2, and 0.8 Gauss/cm), and 21^3 k-space samples were acquired in 18 min. (**B**) The FOV was encoded in 21 gradient steps corresponding to a slice thickness of 2.2 mm. A 3D image was reconstructed on 64^3 matrix, giving a voxel resolution of 0.7 mm^3. A voxel resolution of 0.7 mm^3 with a slice thickness of 2.2 mm implies that three consecutive slices are contained in a slice. Several nonadjacent axial and coronal slices are shown from the 3D pO_2 mapping. Numbers on the image refer to the slice number.

TABLE 1. COMPARISON OF PRSSI AND CTSSI

	PRSSI	*CTSSI*
Gradient coordinate system	Polar	Cartesian
Gradient increment	Depending on pseudo angle α $G_\alpha = \tan\alpha \times \Delta H/\Delta L$	Identical incrementation $G_n = [n - (N + 1)/2] \times G$, (n = 1 to N)
Sweep (band) width	Depending on pseudo angle α $SW_\alpha = \Delta H/\cos\alpha$	Identical for all data $SW = h/(g \cdot \beta \cdot \Delta_T)$
FOV	Flexibility of $\Delta H/\Delta L$ is limited by G_{max}.	$FOV = N \cdot 2\pi/(\gamma_e \cdot \tau_p \cdot G_{max}) = 2\pi/(\gamma_e \cdot \tau_p \cdot \Delta G)$
Image reconstruction	Back-projection based reconstructions	FT (k-space)
Image resolution	Depending on G_{max} and linewidth	Depending on FOV and N
Limitation (impossible data)	$\alpha = 90$ degrees	$\tau_p = 0$ ns
Reason of the limitation	G_α and SW_α are divergent at $\alpha = 90$ degrees	FOV is divergent at $\tau_p = 0$ ns

PRSSI, projection reconstruction spectral-spatial imaging; CTSSI, constant-time spectral-spatial imaging; FOV, field of view.

±90 degrees) in the case of PRSSI, uniform resolution at all delays is difficult in CTSSI because at very short delays, larger gradients will limit the resolution, whereas at large delays for the same gradients, the SNR will be poorer. Obviously, those limitations of data acquisition seem to be parallel in the two methods, and one may not be able to get over the "missing angle" problems.

OMRI

OMRI is a double-resonance technique involving both EPR and NMR, referred to also as PEDRI, in which the native MRI signal is enhanced by the Overhauser effect (90), also known as DNP. In other words, the OMRI is an MRI-based technique that can indirectly provide information relating to the EPR linewidth of the paramagnetic contrast agent. To start with, the spin system of paramagnetic contrast agent (free radicals; *i.e.*, unpaired electrons) coexisting in the sample is saturated by the irradiation of the RF pulse (EPR irradiation). Next, the energy of polarized electron spins transfers to nuclear spins through the electron-relaxation pathway of the paramagnetic contrast agent (mostly *via* electron–nuclear dipolar interaction). Finally, large population differences of energy state of nuclear spins are obtained. Thus, the result is an enhanced NMR signal intensity.

A combination of OMRI and TAM contrast agent provides pO_2 images co-registered with morphologic information (7, 26, 27, 44). The OMRI oximetry, which detects the variation of EPR linewidth of the TAM radical, is based on the EPR oximetry technique. The OMRI oximetry can achieve noninvasive and quantitative oxygen-mapping capabilities with good anatomic information. Figure 13A shows an axial slice of the normal and tumor-bearing thighs of a mouse, which shows an anatomic image with good resolution displaying the heterogeneity of distribution of the paramagnetic contrast agent in the tumor. Figure 13B is a calculated pO_2 mapping using the same data set, exhibiting a low oxygen level in the tumor tissue. The OMRI oximetry required a careful regulation of pharmacokinetics of the TAM radical (71), because a constant concentration of TAM radical in specific regions throughout the data acquisition is necessary. The accumulation or elimination of the TAM radical during the data acquisition could translate to change of pO_2, because the Overhauser enhancement factors depend both on the TAM concentration and on the pO_2. Adequate image intensity for *in vivo* oximetry by OMRI could be achieved only by continuous probe injection, which resulted in 1 m*M* Oxo63 concentration in the blood. A systematic correction of the data,

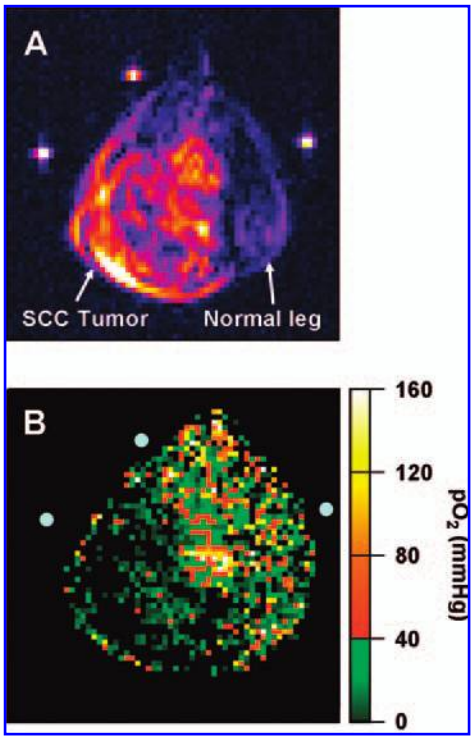

FIG. 13. OMRI oximetry. (**A**) Anatomic information obtained by OMRI. (**B**) Oxygen mapping of the identical slice of **A**. An axial slice of the tumor-bearing and normal legs of a mouse measured by OMRI (TR, 750 ms; TE, 25 ms; T_{EPR}, 500 ms; EPR power, 90 W; N_{EX}, 2; FOV, 32 × 32 mm; slice, 8 mm; and resolution, 64 × 64) 35 min after Oxo63 injection (0.75 μmol/g b.w. bolus injection followed by 0.06 μmol/min/g b.w. continuous injection).

such as the differences in the intrinsic T_1 of the sample, is required for the OMRI oximetry (77). The pO_2 resolution obtained by the OMRI oximetry critically depends on the signal-to-noise ratio (SNR) of the native MRI. The pO_2 resolution obtained by our instrument using 15 mT for MR detection was around ±5 mm Hg. Although the oxygen resolution of OMRI has relatively wider variation compared with the time-domain EPR CTSSI with the multiple G_{max} method (~1 mm Hg), the detailed anatomic information that one can obtain in OMRI is not possible with the EPRI techniques. Fusion of OMRI and time-domain EPRI can resolve problems associated with anatomic co-registration. A combined EPRI/OMRI scanner can use similar magnetic-field amplitudes. A preliminary version of such a scanner is being tested to obtain capabilities of anatomic co-registration by OMRI with spectral (pO_2) information from EPRI.

The use of OMRI for detection of nitoxyl contrast agents was started by Lurie and colleagues from the late 1980s (58, 59). Nitroxyl contrast agents widely used for *in vivo* EPRI or OMRI studies have two- or three-line EPR spectra, whereas most OMRI experiments performed to date have used only a single EPR line. Alecci *et al*. (5) developed a new OMRI apparatus, equipped with a triple-tuned resonator, which was designed for simultaneous excitation of the doublet (^{15}N) or triplet (^{14}N) EPR lines of nitroxyl contrast agents. The details of the EPR hardware used to generate the two or three EPR frequencies were described, and images obtained with simultaneous multiple EPR irradiation were reported (5). The nitroxyl contrast agents have disadvantages for OMRI detection, such as hyperfine splitting and relatively broad linewidth. Lurie and colleagues (60, 61) developed a field-cycled system to achieve a higher magnetic field for MR detection for nitroxyl contrast agents. Very recently, it was made possible with the field-cycled PEDRI to obtain high-quality MRI by switching the B_0 field from 5 mT for EPR to 450 mT for MRI in 40 ms (62).

Utsumi *et al*. (104) proposed a novel imaging technique to separate reduction or oxidation reactions or both, which can simultaneously occur in a sample, using multiple nitroxyl contrast agents labeled by different isotopes (*i.e*., ^{14}N and ^{15}N). They also proposed separate imaging for intra- and extracellular reactions using dual-labeled nitroxyl contrast agents having different membrane permeability. These applications, which could also be addressed by the spectral–spatial EPRI mode, were markedly improved with better temporal resolution and higher spatial resolution and slice selection with OMRI. Zweier and colleagues (55, 56) have worked in the field of cardiology and tried to visualize redox reactions in the cardiovascular systems using EPR, and they developed several EPRI techniques. The EPR-related spectroscopic imaging with high temporal and spatial resolution using the OMRI technique has enabled rapid imaging of free radical metabolisms.

The Overhauser effect is valid not only for proton but also for other nuclides, such as ^{19}F and ^{13}C. Trials to detect ^{19}F tracer compounds using the OMRI instrument, which was also called fluorine electron double-resonance imaging (FEDRI), were reported (79, 81). An endogenous ^{13}C-labeled tracer compound is loaded with paramagnetic species (free radicals) to special hyperpolarizer equipment and hyperpolarized at liquid helium temperature by EPR irradiation to give an enhanced ^{13}C-MRI intensity (28). These techniques can be alternative applications of imaging nuclear probes.

CONCLUSION

EPRI is basically a spatially resolved spectroscopic technique. OMRI and MRI can indirectly detect paramagnetic behavior of free radical contrast agents. Functional information

Table 2. Classification of In Vivo Imaging Techniques and Applications Based on EPR or Paramagnetic Species

Modality	*Detection*	*Dimension*	*Reconstruction*	*Special condition*	*Application*	*References*
EPRI	CW	Spatial	PR		Location mapping	2, 11, 15, 41, 103
				Time course	Redox mapping	39, 43, 51, 52, 106, 108
				RF power series	T_{1e}-based oximetry	8, 33
		Spectral–spatial	PR	Wide spectral window	Separation of several species	69, 72, 73
				Short spectral window	LW-based oximetry	21, 46, 47
		Spectral-spatial	FT (CTSSI)		LW-based oximetry	70
	FID	Spatial	PR		Location mapping	99
		Spatial	FT (SPI)		Location mapping	100
		Spectral-spatial	FT (CTSSI)	Series of SPI and G_{max}	T_{2e}*-based oximetry	74
	Spin-echo	Spectral-spatial	PR	Series of echo times	T_{2e}*-based oximetry	63
OMRI	GRE (MRI)	Spatial (slice)	FT	Time course	Redox mapping	55, 56, 104
			FT	Frequency series	Separation of several species	104
			FT	RF power series	LW-based oximetry	26, 27, 44
(FEDRI)			FT	^{19}F detection	^{19}F compounds	79, 81
MRI	SPGR	Spatial (slice)	FT	Nitroxide, time course	Redox mapping	75
	true FISP	Spatial (slice)	FT	Hyperpolarized ^{13}C	Angiography	28

CW, continuous-wave; EPRI, electron paramagnetic resonance imaging; FID, free induction decay; FT, Fourier transform reconstruction in k-space; GRE, gradient echo; LW, (EPR) linewidth; OMRI, Overhauser enhanced MRI; PR, projection reconstruction; RF, radiofrequency; SPGR, spoiled gradient echo; SPI, single-point imaging.

obtained through the paramagnetic compound (contrast agent), such as EPR linewidth, signal decay, and so on, are spatially resolved using a series of suitably controlled field gradients, RF powers, and acquisitions. It is different from radiologic tomography techniques, which provide pharmacokinetic information to spatial image using molecular probes. Table 2 is a summary of *in vivo* imaging techniques and applications relating to paramagnetic species (*i.e*., EPRI, OMRI, and MRI). Those imaging techniques have the possibility of obtaining maximally 5D information (*i.e*., 3D spatial + 1D spectral + 1D temporal dimensions), theoretically. Researchers should select a modality that addresses a suitable balance of the spectral, spatial dimensionality, and temporal information that is relevant for their specific system.

ACKNOWLEDGMENTS

We appreciate the invitation of Prof. Harold M. Swartz to include us in this special issue of *Antioxidants & Redox Signaling*. Some of illustrations in this review were composed from previous publications of us and others. We thank our colleagues, N. Devasahayam and J. W. Koscielniak, for developing our time-domain and CW EPRI instruments.

ABBREVIATIONS

ART, algebraic reconstruction technique; BOLD-MRI, blood oxygen level–dependent MRI; CT, x-ray computed tomography; CTI, constant-time imaging; CW, continuous-wave; DNP, dynamic nuclear polarization; EPR, electron paramagnetic resonance; EPRI, electron paramagnetic resonance imaging; FBP, filtered back-projection; FEDRI, fluorine electron double-resonance imaging; FID, free induction decay; *f*MRI, functional MRI; FOV, field of view; FT, Fourier transformation; FT-CTSSI, FT constant-time spectral–spatial imaging; MRI, magnetic resonance imaging; OMRI, Overhauser-enhanced MRI; PEDRI, proton electron double-resonance imaging; PRSSI, projection reconstruction spectral–spatial imaging; PET, positron emission tomography; SPECT, single-photon emission computed tomography; SPI, single-point imaging; T_{1e}, T_1 relaxation of electron spin; $T_{2e}{}^*$, $T_2{}^*$ relaxation of electron spin; TAM, triarylmethyl; TOLD-MRI, tissue oxygen level–dependent MRI.

REFERENCES

1. Afeworki M, van Dam GM, Devasahayam N, Murugesan R, Cook J, Coffin D, Ardenkjær-Larsen JH, Mitchell JB, Subramanian S, and Krishna MC. Three-dimensional whole body imaging of spin probes in mice by time-domain radiofrequency electron paramagnetic resonance. *Magn Reson Med* 43: 375–382, 2000.
2. Alecci M, Colacicchi S., Indovina PL, Momo F, Pavone P, and Sotgiu A. Three-dimensional in vivo EPR imaging in rats. *Magn Reson Imaging* 8: 59–63, 1990.
3. Alecci M, Gualtieri G, Sotgiu A, Testa L, and Varoli V. Multipolar magnet for low-frequency ESR imaging. *Measur Sci Technol* 2: 32–37, 1991.
4. Alecci M, Ferrari M, Quaresima V, Sotgiu A, and Ursini CL. Simultaneous 280 MHz EPR imaging of rat organs during nitroxide free radical clearance. *Biophys J* 67: 1274–1279, 1994.
5. Alecci M, Lurie DJ, Nicholson I, Placidi G, and Sotgiu A. A proton-electron double-resonance imaging apparatus with simultaneous multiple electron paramagnetic resonance irradiation at 10 mT. *MAGMA* 4: 187–193, 1996.
6. Alecci M, Brivati JA, Placidi G, and Sotugiu A. A radiofrequency (220-MHz) Fourier transform EPR spectrometer. *J Magn Reson* 130: 272–280, 1998.
7. Ardenkjær-Larsen JH, Laursen I, Leunbach I, Ehnholm G, Wistrand LG, Petersson JS, and Golman K. EPR and DNP properties of certain novel single electron contrast agents intended for oximetric imaging. *J Magn Reson* 133: 1–12, 1998.
8. Bacic G, Demsar F, Zolnai Z, and Swartz HM. Contrast enhancement in ESR imaging: role of oxygen. *Magn Reson Med Biol* 1: 55–65, 1988.
9. Bacic G, Walczak T, Demsar F, and Swartz HM. Electron spin resonance imaging of tissues with lipid-rich areas. *Magn Reson Med* 8: 209–219, 1988.
10. Berliner LJ and Fujii H. Magnetic resonance imaging of biological specimens by electron paramagnetic resonance of nitroxide spin labels. *Science* 227: 517–519, 1985.
11. Berliner LJ, Fujii H, Wan X, and Lukiewicz SJ. Feasibility study of imaging a living murine tumor by electron paramagnetic resonance. *Magn Reson Med* 4: 380–384, 1987.
12. Bernardo ML Jr, Lauterbur PC, and Hedges LK. Experimental example of NMR spectroscopic imaging by projection reconstruction involving and intrinsic frequency dimension. *J Magn Reson* 61: 168–174, 1985.
13. Chzhan M, Shteynbuk M, Kuppusamy P, and Zweier JL. An optimized L-band ceramic resonator for EPR imaging of biological samples. *J Magn Reson A* 105: 49–53, 1993.
14. Chzhan M, Kuppusamy P, and Zweier JL. Development of an electronically tunable L-band resonator for EPR spectroscopy and imaging of biological samples. *J Magn Reson B* 108: 67–72, 1995.
15. Colacicchi S, Indovina PL, Momo F, and Sotgiu A. Low-frequency three-dimensional ESR imaging of large samples. *J Phys E Sci Instrum* 21: 910–913, 1988.
16. Demsar F, Walczak T, Morse PD II, Bacic G, Zolnai Z, and Swartz HM. Detection of diffusion and distribution of oxygen by fast-scan EPR imaging. *J Magn Reson* 76: 224–231, 1988.
17. Deng Y, He G, Petryakov S, Kuppusamy P, and Zweier JL. Fast EPR imaging at 300 MHz using spinning magnetic field gradients. *J Magn Reson* 168: 220–227, 2004.
18. Devasahayam N, Subramanian S, Murugesan R, Cook JA, Afeworki M, Tschudin RG, Mitchell JB, and Krishna MC. Parallel coil resonators for time-domain radiofrequency electron paramagnetic resonance imaging of biological objects. *J Magn Reson* 142: 168–176, 2000.
19. Eaton GR and Eaton SS. Electron spin-echo-detected EPR imaging. *J Magn Reson* 67: 73–77, 1986.
20. Eaton GR and Eaton SS. EPR imaging using T_1 selectivity. *J Magn Reson* 71: 271–275, 1987.
21. Elas M, Williams BB, Parasca A, Mailer C, Pelizzari CA, Lewis MA, River JN, Karczmar GS, Barth ED, and Halpern HJ. Quantitative tumor oxymetric images from 4D electron paramagnetic resonance imaging (EPRI): methodology and comparison with blood oxygen level-dependent (BOLD) MRI. *Magn Reson Med* 49: 682–691, 2003.
22. Emid S and Creyghton JHN. High-resolution NMR imaging in solid. *Physica B C* 128: 81–83, 1985.
23. Ewert U and Herrling T. Spectrally resolved EPR tomography with stationary gradient. *Chem Phys Lett* 129: 516–520, 1986.
24. Froncisz W, Oles T, and Hyde JS. Murine L-band ESR loop-gap resonator. *J Magn Reson* 82: 109–114, 1989.
25. Goda F, Liu KJ, Walczak T, O'Hara JA, Jiang J, and Swartz HM. In vivo oximetry using EPR and India ink. *Magn Reson Med* 33:237–245, 1995.
26. Golman K, Leunbach I, Ardenkj[ae]r-Larsen JH, Ehnholm GJ, Wistrand LG, Petersson JS, Jarvi A, and Vahasalo S. Overhauser-enhanced MR imaging (OMRI). *Acta Radiol* 39: 10–17, 1998.

27. Golman K, Petersson JS, Ardenkjær-Larsen JH, Leunbach I, Wistrand LG, Ehnholm G, and Liu K. Dynamic in vivo oxymetry using Overhauser enhanced MR imaging. *J Magn Reson Imaging* 12: 929–938, 2000.
28. Golman K, Ardenkjær-Larsen JH, Petersson JS, Mansson S, and Leunbach I. Molecular imaging with endogenous substances. *Proc Natl Acad Sci U S A* 100: 10435–10439, 2003.
29. Halpern HJ, Spencer DP, van Polen J, Bowman MK, Nelson AC, Dowey EM, and Teicher BA. Imaging radio frequency electron-spin-resonance spectrometer with high resolution and sensitivity for in vivo measurements. *Rev Sci Instrum* 60: 1040–1050, 1989.
30. Halpern HJ, Yu C, Peric M, Barth E, Grdina DJ, and Teicher BA. Oxymetry deep in tissues with low-frequency electron paramagnetic resonance. *Proc Natl Acad Sci U S A* 91: 13047–13051, 1994.
31. Halpern HJ, Peric M, Yu C, Barth ED, Chandramouli GVR, Makinen MW, and Rosen GM. In vivo spin-label murine pharmacodynamics using low-frequency electron paramagnetic resonance imaging. *Biophys J* 71: 403–409, 1996.
32. Halse M, Goodyear DJ, MacMillan B, Szomolanyi P, Matheson D, and Balcom BJ. Centric scan SPRITE magnetic resonance imaging. *J Magn Reson* 165: 219–229, 2003.
33. Hama Y, Matsumoto K, Subramanian S, Devasahayam N, Koscielniak JW, Hyodo F, Sowers A, Cook JA, Mitchell JB, and Krishna MC. Continuous wave EPR oximetric imaging using radiofrequency power saturation effects: EPR-2005 a joint conference of 11th in vivo EPR spectroscopy and imaging and 8th international EPR spin trapping, Columbus, OH: 2005, pp. 4–8.
34. He G, Shankar RA, Chzhan M, Samouilov A, Kuppusamy P, and Zweier JL. Noninvasive measurement of anatomic structure and intraluminal oxygenation in the gastrointestinal tract of living mice with spatial and spectral EPR imaging. *Proc Natl Acad Sci U S A* 96: 4586–4591, 1999.
35. Hoch MJR. Electron spin resonance imaging of paramagnetic centres in solids. *J Phys C Solid State Phys* 14: 5659–5666, 1981.
36. Hoch MJR and Day AR. Imaging of paramagnetic centers in diamond. *Solid State Commun* 30: 211–213, 1979.
37. Hornak JP, Moscicki JK, Schneider DJ, and Freed JH. Diffusion coefficients in anisotropic fluids by ESR imaging of concentration profiles. *J Chem Phys* 84: 3387–3395, 1986.
38. Ikeya M and Miki T. ESR microscopic imaging with microfabricated field gradient coils. *Jpn J Appl Phys* 26: L929–L931, 1987.
39. Ilangovan G, Li H, Zweier JL, Krishna MC, Mitchell JB, and Kuppusamy P. In vivo measurement of regional oxygenation and imaging of redox status in RIF-1 murine tumor: effect of carbogen-breathing. *Magn Reson Med* 48: 723–730, 2002.
40. Ilangovan G, Manivannan A, Li H, Yanagi H, Zweier JL, and Kuppusamy P. A naphthalocyanin-based EPR probe for focalized measurements of tissue oxygenation. *Free Radic Biol Med* 32: 139–147, 2002.
41. Ishida S, Matsumoto S, Yokoyama H, Mori N, Kumashiro H, Tsuchihashi N, Ogata T, Yamada M, Ono M, Kitajima T, Kamada H, and Yoshida E. An ESR-CT imaging of the head of a living rat receiving an administration of a nitroxide radical. *Magn Reson Imaging* 10: 109–114, 1992.
42. Karthe W and Wehrsdorfer E. The measurement of inhomogeneous distributions of paramagnetic centers by means of EPR. *J Magn Reson* 33: 107–111, 1979.
43. Kazama S, Takashige G, Yoshioka H, Tanizawa H, Ogata T, Koscielniak J, and Berliner LJ. Dynamic electron spin resonance (ESR) imaging of the distribution of spin labeled dextran in mouse. *Magn Reson Med* 36: 547–550, 1996.
44. Krishna MC, English S, Yamada K, Yoo J, Murugesan R, Devasahayam N, Cook JA, Golman K, Ardenkjaer-Larsen JH, Subramanian S, and Mitchell JB. Overhauser enhanced magnetic resonance imaging for tumor oximetry: coregistration of tumor anatomy and tissue oxygen concentration. *Proc Natl Acad Sci U S A* 99: 2216–2221, 2002.
45. Kuppusamy P and Zweier, JL. A forward-subtraction procedure for removing hyperfine artifacts in electron paramagnetic resonance imaging. *J Magn Reson* 35: 316–332, 1996
46. Kuppusamy P, Chzhan M, Vij K, Shteynbuk M, Jefer DJ, Giannella E, and Zweier JL. Three-dimensional spectral-spatial EPR imaging of free radicals in the heart: a technique for imaging tissue metabolism and oxygenation. *Proc Natl Acad Sci U S A* 91: 3388–3392, 1994.
47. Kuppusamy P, Chzhan M, and Zweier JL. Development and optimization of three-dimensional spatial EPR imaging for biological organs and tissues. *J Magn Reson B* 106: 122–130, 1995.
48. Kuppusamy P, Chzhan M, Samouilov A, Wang P, and Zweier JL. Mapping the spin-density and lineshape distribution of free radicals using 4D spectral-spatial EPR imaging. *J Magn Reson B* 107: 116–125, 1995.
49. Kuppusamy P, Wang P, Zweier JL, Krishna MC, Mitchell JB, Ma L, Trimble CE, and Hsia CJC. Electron paramagnetic resonance imaging of rat heart with nitroxide and polynitroxyl-albumin. *Biochemistry* 35: 7051–7057, 1996.
50. Kuppusamy P, Wang P, Chzhan M, and Zweier JL. High resolution electron paramagnetic resonance imaging of biological samples with a single line paramagnetic label. *Magn Reson Med* 37: 479–483, 1997.
51. Kuppusamy P, Afeworki M, Shankar RA, Coffin D, Krishna MC, Hahn SM, Mitchell JB, and Zweier JL. In vivo electron paramagnetic resonance imaging of tumor heterogeneity and oxygenation in a murine model. *Cancer Res* 58: 1562–1568, 1998.
52. Kuppusamy P, Li H, Ilangovan G, Cardounel AJ, Zweier JL, Yamada K, Krishna MC, and Mitchell JB. Noninvasive imaging of tumor redox status and its modification by tissue glutathione levels. *Cancer Res* 62: 307–312, 2002.
53. Lauterbur PC. Image formation by induced local interactions: examples employing nuclear magnetic resonance. *Nature* 242: 190–191, 1973.
54. Lauterbur PC, Levin DN, Marr RB. Theory and simulation of NMR spectroscopic imaging and field plotting by projection reconstruction involving and intrinsic frequency dimension. *J Magn Reson* 59: 536–541, 1984.
55. Li H, He G, Deng Y, Kuppusamy P, and Zweier JL. In vivo proton electron double resonance imaging of the distribution and clearance of nitroxide radicals in mice. *Magn Reson Med* 55: 669–675, 2006.
56. Liebgott T, Li H, Deng Y, and Zweier JL. Proton electron double resonance imaging (PEDRI) of the isolated beating rat heart. *Magn Reson Med* 50: 391–399, 2003.
57. Liu KJ, Gast P, Moussavi M, Norby SW, Vahidi N, Walczak T, Wu M, Swartz HM. Lithium phthalocyanine: a probe for electron paramagnetic resonance oximetry in viable biological systems. *Proc Natl Acad Sci U S A* 90: 5438–5442, 1993.
58. Lurie DJ, Bussell DM, Bell LH, and Malard JR. Proton electron double resonance imaging of free radical solutions. *J Magn Reson* 76: 366–370, 1988.
59. Lurie DJ, Nicholson I, Foster MA, and Mallard JR. Free radicals imaged in vivo in the rat by using proton-electron double-resonance imaging. *Phil Trans R Soc Lond* A333, 453–456, 1990.
60. Lurie DJ, Foster MA, Yeung D, and Hutchison JM. Design, construction and use of a large-sample field-cycled PEDRI. *Phys Med Biol* 43: 1877–1886, 1998.
61. Lurie DJ, Li H, Petryakov S, and Zweier JL. Development of a PEDRI free-radical imager using a 0.38 T clinical MRI system. *Magn Reson Med* 47: 181–186, 2002.
62. Lurie DJ, Davies GR, Foster MA, and Hutchison JMS. Field-cycled PEDRI imaging of free radicals with detection at 450 mT. *Magn Reson Imaging* 23: 175–181, 2005.
63. Mailer C, Sundramoorthy SV, Pelizzari CA, and Halpern HJ. Spin echo spectroscopic electron paramagnetic resonance imaging. *Magn Reson Med* 55: 904–912, 2006.
64. Maltempo MM. Differentiation of spectral and spatial components in EPR imaging using 2D image reconstruction algorithms. *J Magn Reson* 69: 156–161, 1986.
65. Maltempo MM, Eaton SS, and Eaton GR. Spectral-spatial two-dimensional EPR imaging. *J Magn Reson* 72: 449–455, 1987.
66. Maltempo MM, Eaton SS, and Eaton GR. Reconstruction of spectral-spatial two-dimensional EPR images from incomplete sets of projections without prior knowledge of the component spectra. *J Magn Reson* 77: 75–83, 1988.

67. Maltempo MM, Eaton SS, and Eaton GR. Artifacts in spectral-spatial EPR images of portions of spectra. *J Magn Reson* 85: 303–313, 1989.
68. Maresch GG, Mehring M, and Emid S. High-resolution electron-spin-resonance imaging. *Physica B C* 138: 261–263, 1986.
69. Matsumoto K and Utsumi H. Development of separable electron spin resonance-computed tomography imaging for multiple radical species: an application to (OH and (NO. *Biophys J* 79: 3341–3349, 2000.
70. Matsumoto K, Chandrika B, Lohman JAB, Mitchell JB, Krishna MC, and Subramanian S. Application of continuous-wave EPR spectral-spatial image reconstruction techniques for in vivo oxymetry: comparison of projection reconstruction and constant-time modalities. *Magn Reson Med* 50: 865–874, 2003.
71. Matsumoto K, English S, Yoo J, Yamada K, Devasahayam N, Cook JA, Mitchell JB, Subramanian S, and Krishna MC. Pharmacokinetics of a triarylmethyl-type paramagnetic spin probe used in EPR oximetry. *Magn Reson Med* 52: 885–892, 2004.
72. Matsumoto K, Yahiro T, Yamada K, and Utsumi H. In vivo EPR spectroscopic imaging for a liposomal drug delivery system. *Magn Reson Med* 53: 1158–1165, 2005.
73. Matsumoto K, Kawai S, Chignell CF, and Utsumi H. Location of anthralin radical generation in mouse skin by UV-A irradiation: an estimation using microscopic EPR spectral-spatial imaging. *Magn Reson Med* 55: 738–742, 2006.
74. Matsumoto K, Subramanian S, Devasahayam N, Aravalluvan T, Murugesan R, Cook JA, Mitchell JB, and Krishna MC. Electron paramagnetic resonance imaging of tumor hypoxia: enhanced spatial and temporal resolution for in vivo pO2 determination. *Magn Reson Med* 55: 1157–1163, 2006.
75. Matsumoto K, Hyodo F, Matsumoto A, Koretsky AP, Sowers AL, Mitchell JB, and Krishna MC. High resolution mapping of tumor redox status by magnetic resonance imaging using nitroxides as redox-sensitive contrast agents. *Clin Cancer Res* 12: 2455–2462, 2006.
76. Matsumoto K, Bernardo M, Subramanian S, Choyke P, Mitchell JB, Krishna MC, and Lizak MJ. MR assessment of changes of tumor in response to hyperbaric oxygen treatment. *Magn Reson Med Magn Reson Med* 56: 240–246, 2006.
77. Matsumoto S, Utsumi H, Aravalluvan T, Matsumoto K, Matsumoto A, Devasahayam N, Sowers AL, Mitchell JB, Subramanian S, and Krishna MC. Influence of proton T1 on oxymetry using Overhauser enhanced magnetic resonance imaging. *Magn Reson Med* 54: 213–217, 2005.
78. Miki T and Ikeya M. Electron spin resonance microscopy by localized magnetic field modulation. *Jpn J Appl Phys* 26: L1495–L1498, 1987.
79. Modica A, Lurie DJ, and Alecci M. Sequential, co-registered fluorine and proton field-cycled Overhauser imaging at a detection field of 59 mT. *Phys Med Biol* 51: N39–N45, 2006.
80. Murugesan R, Cook JA, Devasahayam N, Afeworki M, Subramanian S, Tschudin R, Larsen JHA, Mitchell JB, Russo A, and Krishna M. In vivo imaging of a stable paramagnetic probe by pulsed-radiofrequency electron paramagnetic resonance spectroscopy. *Magn Reson Med* 38: 409–414, 1997.
81. Murugesan R, English S, Reijnders K, Yamada K, Cook JA, Mitchell JB, Subramanian S, and Krishna MC. Fluorine electron double resonance imaging for ^{19}F MRI in low magnetic fields. *Magn Reson Med* 48: 523–529, 2002.
82. Nishikawa H, Fujii H, and Berliner LJ. Helices and surface coils for low-field in vivo ESR and EPR imaging applications. *J Magn Reson* 62: 79–86, 1985.
83. Ogata T, Ono M, Fujisawa T, Yoshida E, and Kamada H. An example of in vivo analysis by L-band ESR technique using a loop-gap resonator. *Chem Lett* 1986: 1681–1684, 1986.
84. Ogawa S, Lee TM, Nayak AS, and Glynn P. Oxygenation-sensitive contrast in magnetic resonance image of rodent brain at high magnetic fields. *Magn Reson Med* 14: 68–78, 1990.
85. Ohno K. A method of EPR imaging: application to spatial distributions of hydrogen atoms trapped in sulfuric acid ices. *Jpn J Appl Phys* 20: L179–L182, 1981.
86. Ohno K. ESR imaging: a deconvolution method for hyperfine patterns. *J Magn Reson* 50: 145–150, 1982.
87. Ohno K and Murakami T. Microscopic ESR imaging using a microcoil system. *J Magn Reson* 79: 343–347, 1988.
88. Ohno K and Watanabe M. Electron paramagnetic resonance imaging using magnetic-field-gradient spinning. *J Magn Reson* 143: 274–279, 2000.
89. Ohno K, Yonezawa J, and Morita Y. Electron spin resonance imaging study of spatial distribution of paramagnetic species produced by γ-irradiation in sulfuric acid ices. *J Phys Chem* 93: 1657–1660, 1989.
90. Overhauser AW. Polarization of nuclei in metals. *Phys Rev* 92: 411–415, 1953.
91. Placidi G, Alecci M, Colacicchi S, and Sotgiu A. Fourier reconstruction as a valid alternative to filtered back projection in iterative applications: implementation of Fourier spectral spatial EPR imaging. *J Magn Reson* 134: 280–286, 1998.
92. Placidi G, Brivati JA, Alecci M, Testa L, and Sotgiu A. Two-dimensional 220 MHz Fourier transform EPR imaging. *Phys Med Biol* 43: 1845–1850, 1998.
93. Sano H, Naruse M, Matsumoto K, Oi T, and Utsumi H. A new nitroxyl-probe with high retention in the brain and its application for brain imaging. *Free Radic Biol Med* 28: 959–969, 2000.
94. Sendhil V, Spencer RGS, Zweier JL, and Kuppusamy P. Electron paramagnetic resonance oxygen mapping (EPROM): direct visualization of oxygen concentration in tissue. *Magn Reson Med* 43: 804–809, 2000.
95. Sotgiu A. Resonator design for in vivo ESR spectroscopy. *J Magn Reson* 65: 206–214, 1985.
96. Stemp EDA, Eaton GR, Eaton SS, and Maltempo MM. Spectral-spatial electron paramagnetic resonance imaging and transport of radicals in nonuniform media. *J Phys Chem* 91: 6467–6469, 1987.
97. Stillman AE, Levin DN, Yang DB, Marr RB, and Lauterbur PC. Back projection reconstruction of spectroscopic NMR images from incomplete sets of projections. *J Magn Reson* 69: 168–175, 1986.
98. Subramanian S, Murugesan R, Devasahayam N, Cook JA, Afeworki M, Pohida T, Tschudin RG, Mitchell JB, and Krishna MC. High-speed data acquisition system and receiver configurations for time-domain radiofrequency electron paramagnetic resonance spectroscopy and imaging. *J Magn Reson* 137: 379–388, 1999.
99. Subramanian S, Yamada K, Irie A, Murugesan R, Cook JA, Devasahayam N, Van Dam GM, Mitchell JB, Krishna MC. Noninvasive in vivo oximetric imaging by radiofrequency FT EPR. *Magn Reson Med* 47: 1001–1008, 2002
100. Subramanian S, Devasahayam N, Murugesan R, Yamada K, Cook J, Taube A, Mitchell JB, Lohman JAB, and Krishna MC. Single-point (constant-time) imaging in radiofrequency Fourier transform electron paramagnetic resonance. *Magn Reson Med* 48: 370–379, 2002.
101. Subramanian S, Matsumoto K, Mitchell JB, and Krishna MC. Radio frequency continuous-wave and time-domain EPR imaging and Overhauser-enhanced magnetic resonance imaging of small animals: instrumental developments and comparison of relative merits for functional imaging. *NMR Biomed* 17: 263–294, 2004.
102. Sueki M, Eaton GR, and Eaton SS. Electron spin echo and CW perspectives in 3D EPR imaging. *Appl Magn Reson* 1: 20–28, 1990.
103. Takeshita K, Utsumi H, and Hamada A. ESR measurement of radical clearance in lung of whole mouse. *Biochem Biophys Res Commun* 177: 874–880, 1991.
104. Utsumi H, Yamada K, Ichikawa K, Sakai K, Kinoshita Y, Matsumoto S, and Nagai M. Simultaneous molecular imaging of redox reactions monitored by Overhauser-enhanced MRI with ^{14}N- and ^{15}N-labeled nitroxyl radicals. *Proc Natl Acad Sci U S A* 103: 1463–1468, 2006.
105. Wind RA and Ardenkj[ae]r-Larsen JH. ^{1}H DNP at 1.4 T of water doped with a triarylmethyl-based radical. *J Magn Reson* 141: 347–354, 1999.
106. Yamada K, Kuppusamy P, English S, Yoo J, Irie A, Subramanian S, Mitchell JB, and Krishna MC. Feasibility and assessment of non-invasive in vivo redox status using electron paramagnetic resonance imaging. *Acta Radiol* 43: 433–440, 2002.
107. Yamada K, Murugesan R, Devasahayam N, Cook JA, Mitchell JB, Subramanian S, and Krishna MC. Evaluation and comparison

of pulsed and continuous wave radiofrequency electron paramagnetic resonance techniques for in vivo detection and imaging of free radicals. *J Magn Reson* 154: 287–297, 2002.
108. Yokoyama H, Ogata T, Tsuchihashi N, Hiramatsu M, and Mori N. A spatiotemporal study on the distribution of intraperitoneally injected nitroxide radical in the rat head using an in vivo ESR imaging system. *Magn Reson Imaging* 14: 559–563, 1996.
109. Zweier JL, Chzhan M, Evert U, Schneider G, and Kuppusamy P. Development of a highly sensitive probe for measuring oxygen in biological tissues. *J Magn Reson B* 105: 52–57, 1994.

Address reprint requests to:
Murali C. Krishna
Building 10, Room B3 B69
NIH
Bethesda, MD 20892-1002

E-mail: murali@helix.nih.gov

Date of first submission to ARS Central, March 1, 2007; date of final revised submission, March 1, 2007; date of acceptance, March 8, 2007.

This article has been cited by:

1. Kazuhiro Ichikawa, Keiji Yasukawa. 2012. Imaging in vivo redox status in high spatial resolution with OMRI. *Free Radical Research* **46**:8, 1004-1010. [CrossRef]
2. Ly-Binh-An Tran, Anne Bol, Daniel Labar, Bénédicte Jordan, Julie Magat, Lionel Mignion, Vincent Grégoire, Bernard Gallez. 2012. Hypoxia imaging with the nitroimidazole 18F-FAZA PET tracer: A comparison with OxyLite, EPR oximetry and 19F-MRI relaxometry. *Radiotherapy and Oncology* . [CrossRef]
3. Martyna Elas, Kazuhiro Ichikawa, Howard J. Halpern. 2012. Oxidative Stress Imaging in Live Animals with Techniques Based on Electron Paramagnetic Resonance. *Radiation Research* **177**:4, 514-523. [CrossRef]
4. David Bardelang, Micaël Hardy, Olivier Ouari, Paul TordoSpin Labels and Spin Probes . [CrossRef]
5. Mark D. Lingwood, Andrew J. Sederman, Mick D. Mantle, Lynn F. Gladden, Songi Han. 2012. Overhauser dynamic nuclear polarization amplification of NMR flow imaging. *Journal of Magnetic Resonance* . [CrossRef]
6. Zhivko Zhelev, Veselina Gadjeva, Ichio Aoki, Rumiana Bakalova, Tsuneo Saga. 2012. Cell-penetrating nitroxides as molecular sensors for imaging of cancer in vivo, based on tissue redox activity. *Molecular BioSystems* **8**:10, 2733. [CrossRef]
7. Sankaran Subramanian, Nallathamby Devasahayam, Alan McMillan, Shingo Matsumoto, Jeeva P. Munasinghe, Keita Saito, James B. Mitchell, Gadisetti V.R. Chandramouli, Murali C. Krishna. 2011. Reporting of quantitative oxygen mapping in EPR imaging. *Journal of Magnetic Resonance* . [CrossRef]
8. Gareth R. Eaton, Sandra S. EatonElectron Paramagnetic Resonance Imaging . [CrossRef]
9. Valery V. Khramtsov, George L. Caia, Keerthi Shet, Eric Kesselring, Sergey Petryakov, Jay L. Zweier, Alexandre Samouilov. 2010. Variable Field Proton–Electron Double-Resonance Imaging: Application to pH mapping of aqueous samples. *Journal of Magnetic Resonance* **202**:2, 267-273. [CrossRef]
10. Przemyslaw M. Plonka. 2009. Electron paramagnetic resonance as a unique tool for skin and hair research. *Experimental Dermatology* **18**:5, 472-484. [CrossRef]
11. Aya Okajo, Iori Ui, Sushma Manda, Ikuo Nakanishi, Ken-ichiro Matsumoto, Kazunori Anzai, Kazutoyo Endo. 2009. Intracellular and Extracellular Redox Environments Surrounding Redox-Sensitive Contrast Agents under Oxidative Atmosphere. *Biological & Pharmaceutical Bulletin* **32**:4, 535-541. [CrossRef]
12. GuoPing Yan, Lei Peng, ShuangQuan Jian, Liang Li, Steven Eric Bottle. 2008. Spin probes for electron paramagnetic resonance imaging. *Chinese Science Bulletin* **53**:24, 3777-3789. [CrossRef]
13. Deepti S. Vikram, Rizwan Ahmad, Brian K. Rivera, Periannan Kuppusamy. 2008. Mapping of Oxygen Concentration in Biological Samples Using EPR Imaging. *Israel Journal of Chemistry* **48**:1, 39-43. [CrossRef]
14. Roger G Evans, Bruce S Gardiner, David W Smith, Paul M O'Connor. 2008. METHODS FOR STUDYING THE PHYSIOLOGY OF KIDNEY OXYGENATION. *Clinical and Experimental Pharmacology and Physiology* . [CrossRef]
15. Subhojit Som, Lee C. Potter, Rizwan Ahmad, Deepti S. Vikram, Periannan Kuppusamy. 2008. EPR oximetry in three spatial dimensions using sparse spin distribution. *Journal of Magnetic Resonance* **193**:2, 210-217. [CrossRef]
16. Mark W. Dewhirst, Yiting Cao, Benjamin Moeller. 2008. Cycling hypoxia and free radicals regulate angiogenesis and radiotherapy response. *Nature Reviews Cancer* **8**:6, 425-437. [CrossRef]
17. Harold M. Swartz . 2007. On Tissue Oxygen and Hypoxia. *Antioxidants & Redox Signaling* **9**:8, 1111-1114. [Citation] [Full Text PDF] [Full Text PDF with Links]